

Simulation of ship navigation in ice rubble based on peridynamics

R.W. Liu, Y.Z. Xue ^{*}, X.K. Lu, W.X. Cheng

College of Shipbuilding Engineering, Harbin Engineering University, Harbin 150001, PR China

ARTICLE INFO

Keywords:

Peridynamics
Ice load
Ice breaking
Ship–ice interaction
Ice rubble
Voronoi diagram

ABSTRACT

Peridynamic theory has been applied satisfactorily to crack and damage in massive materials and structures. The use of peridynamics to calculate ice loads and simulate the ship–ice interaction process is introduced. The ice–material property, ice–rubble model, and the ship–ice contact model for the calculation program are investigated. Several cases are studied in terms of different ice rubble sizes, concentrations of ice rubble, and sailing speeds. Major characteristics can be obtained, including dynamic crack generation and propagation of ice rubble, and sliding, rotation and accumulation of broken ice; these are observed commonly in polar and Arctic activities. Crack generation and propagation are obtained naturally without setting extra criteria for crack extension, pre-existing crack routes, or crack branching. The capability of this approach is validated by comparison with available experimental results for calculating ice load and the ice–breaking process.

1. Introduction

Arctic activities increasingly frequent. Global warming has made the Arctic regions more attractive for oil and gas exploitation. The shrinking Arctic ice cover will soon make resources more accessible (Kwok and Cunningham, 2012). Shipping lanes in Arctic regions are opening, reducing costs and the risks of access. This is advantageous not only for energy companies engaged in oil and gas exploration and production, but also for shipping and ship building/offshore plants, companies producing icebreakers and ice-going vessels (Kim et al., 2013). The investigation ice load exerted on ice-going vessels and offshore structures is a key part of polar and Arctic activity, and it is also important in ship design (Kujala, 1991; Jia et al., 2009). Matlock et al. (1969) proposed a model of ice structure interaction, and Eranti (1991, 1992) later improved the model. Aksnes (2010) proposed a simplified model of a ship in level ice, decomposing the ice force into destructive, overturning and slip forces. A full-scale test is currently the fastest method to identify the ice load on icebreakers. This produces reliable and accurate data, but it is costly, and unrepeatable, making it unrealistic as a general approach to calculate ice load. Correlation studies between experimental results with refrigerated ice and synthetic ice have been conducted (Song et al., 2007; Kim et al., 2009), and good agreement has been found. Model tests in ice tanks are most commonly used to deal with the ice loads, but they are time-consuming and expensive, especially for the development of optimum hull forms (Kim et al., 2013). Fortunately, ice–ship interaction modeling using numerical methods has been shown to be both efficient and

accurate, both in theoretical research and engineering application. The LS-DYNA finite element program has been successfully applied to structural and flow analysis problems (Derradjı-Aouat and Wang, 2010). A numerical model for real-time simulation of ship–ice interaction developed by Lubbad and Løset (2011) shows the accuracy of numerical models. Correlation studies extend to comparisons between experimental results and numerical analysis based on the fluid–structure interaction method, used by Kim et al. (2013).

Despite the development of many important concepts to predict crack initiation and its growth in materials and structures, it is still a major challenge within the framework of classical continuum mechanics. The main difficulty lies in the mathematical formulation, which assumes that a body remains continuous as it deforms. Therefore, the basic mathematical structure of the formulation breaks down whenever a discontinuity appears in a body. Mathematically, the classical theory is formulated using spatial partial differential equations, and these spatial derivatives are undefined at discontinuities. This introduces an inherent limitation to the classical theory, as the spatial derivatives in the governing equations, by definition, lose their meaning in the presence of a discontinuity, such as a crack (Madenci and Oterkus, 2014). Because traditional numerical methods such as the finite element and boundary methods rarely obtain solutions to these problems, a mesh-free method seems more appropriate. To develop an accurate numerical model and obtain reliable results in numerical simulation, the material–failure model should satisfy two main criteria (Das et al., 2014). First, the model must be able to predict the correct stresses and strains in failure. Second,

* Corresponding author.

E-mail address: xueyanzhuo@hrbeu.edu.cn (Y.Z. Xue).

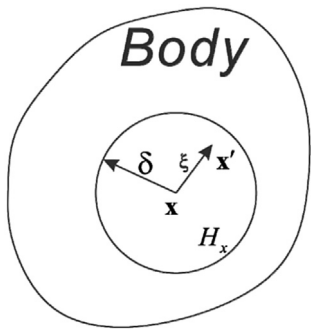


Fig. 1. Each point x in the body interacts directly with points in the sphere H_x through bonds.

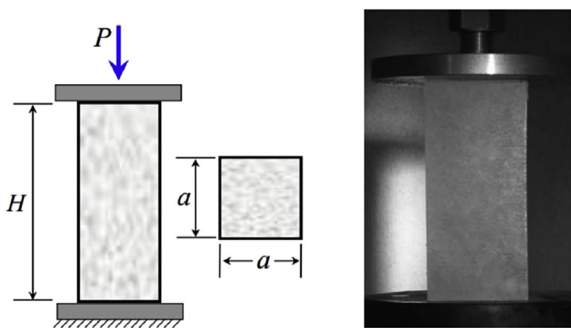


Fig. 2. Uniaxial compression test.

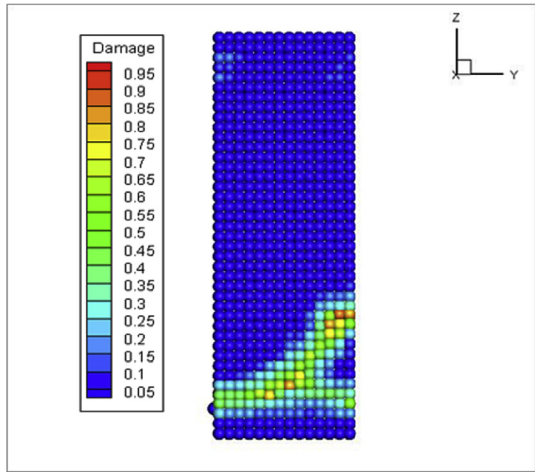


Fig. 3. Simulation of the uniaxial compression test.

the predicted failure mechanism and fracture pattern must be in accordance with those found in experiments. The finite element method, as the leading numerical method, was first used to simulate the fracture of ice, but the difference between the continuity assumption and the real fracture model of the ice caused the difficulty in dealing with the generation and extension cracks (Daley et al., 1998). A discrete method has advantages for modeling the discontinuous phase of the fracture process, but accuracy problems during the continuous phase make it unreliable for modeling the whole process, from continuous to discontinuous. Due to its independence from element grids during computation, a mesh-free method is suitable in the calculation of ice load and modeling ice-ship interactions. A new mesh-free method called peridynamics was coined by Silling in 1998. This theory is a reformulation of the classical continuum mechanics that employs a nonlocal model to describe material properties

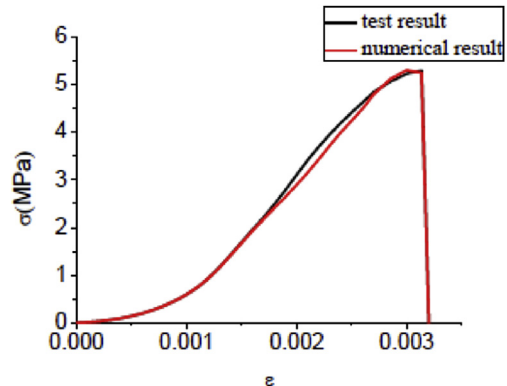


Fig. 4. Stress-strain curve.

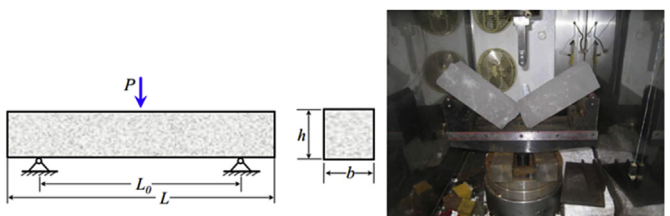


Fig. 5. Three-point bending model test.

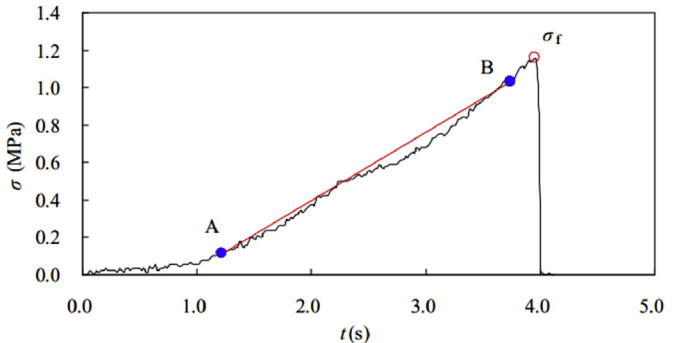


Fig. 6. Stress-time curve of three-point bending model test.

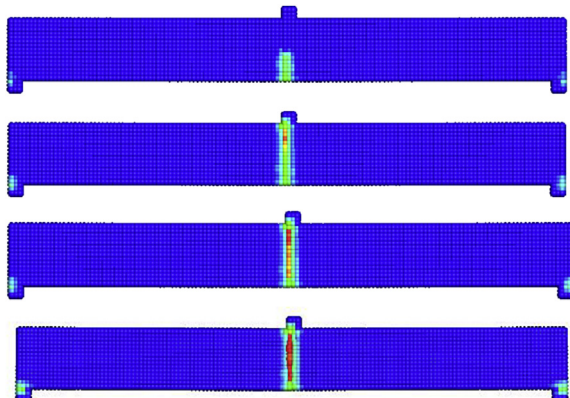


Fig. 7. Simulation of the three-point bending test.

(Silling, 1998, 2000; Silling and Askari, 2005). It assumes that particles in a continuum interact across a finite distance, and it formulates problems in terms of integral equations rather than partial differential

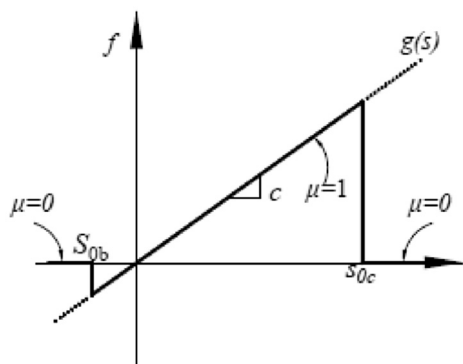


Fig. 8. Bond force as a function of bond stretch in the ice material model.

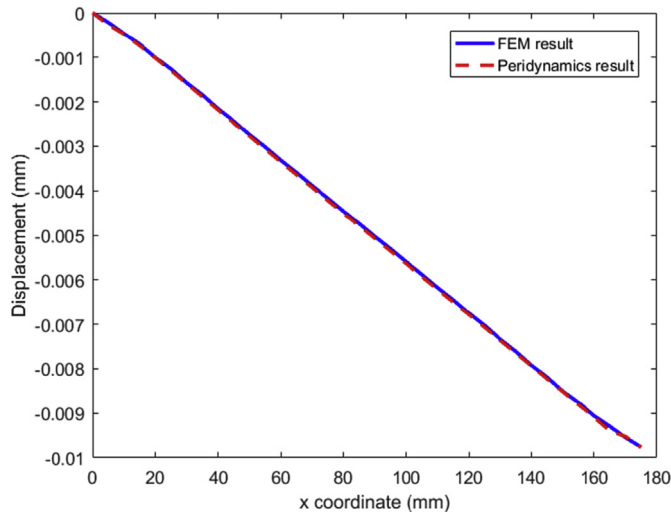


Fig. 9. Comparison of the displacement variations along the center lines under uniaxial compression test using peridynamics and FEM.

equations. Peridynamics manifests its unique superiority in addressing discontinuous problems, which can be introduced to the calculation and simulation of ice loads and ice–ship interactions.

In the present investigation, peridynamics is applied for the first time in the calculation of ice loads and the simulation of the ice–ship interaction process. The basic peridynamics theory is introduced, including the peridynamics model of a continuum; and constitutive modeling that obtains the microscopic parameters and the description of failure. A uniaxial compression test and three-point bending test have been conducted to achieve the appropriate micro-parameters. Ice rubble is produced using a Voronoi diagram algorithm. A ship–ice contact model is developed in this work, and a technique for peridynamics family members search is introduced. Finally, several numerical simulations are conducted to validate the feasibility of this approach.

2. Bond-based peridynamics

Peridynamics was proposed by Silling in 1998 as a reformulation of elasticity theory for discontinuities and long-range forces, which are like molecular dynamics in the continuum situation (Silling, 2000). In bond-based peridynamics, the kinetic equation of particle at \mathbf{x} in the reference configuration at time t is

$$\rho(\mathbf{x})\ddot{\mathbf{u}}(\mathbf{x}, t) = \int_{H_x} \mathbf{f}(\mathbf{u}' - \mathbf{u}, \mathbf{x}' - \mathbf{x}, t) dV_{\mathbf{x}'} + \mathbf{b}(\mathbf{x}, t) \quad (1)$$

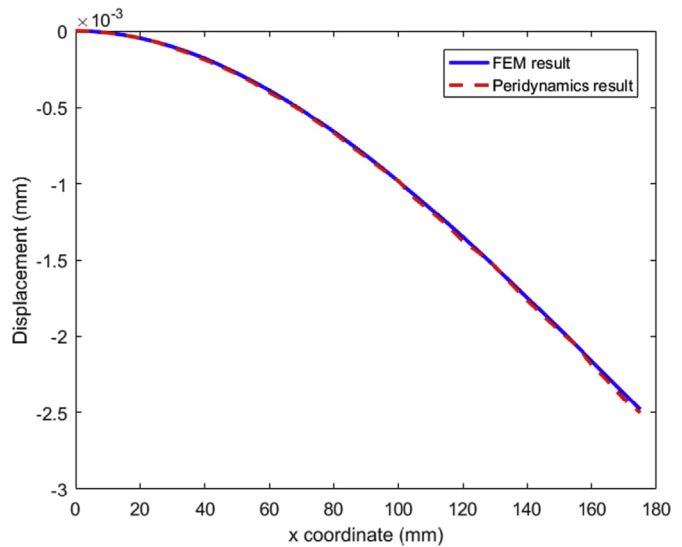


Fig. 10. Comparison of the displacement variations along the center lines in cantilever beam test using peridynamics and FEM.

where H_x is a neighborhood of \mathbf{x} , \mathbf{u} is the displacement vector field, \mathbf{b} is a prescribed body force density field, ρ is the mass density in the reference configuration, and \mathbf{f} is a pairwise force density function whose value is the force vector that material point \mathbf{x}' exerts on material point \mathbf{x} .

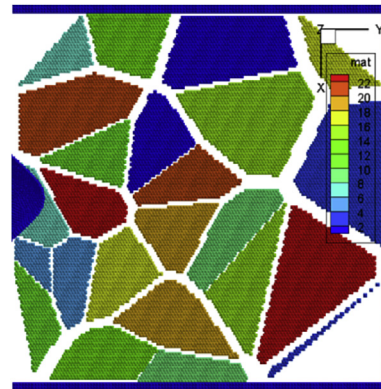


Fig. 11. Diagram of channel covered with ice rubble.

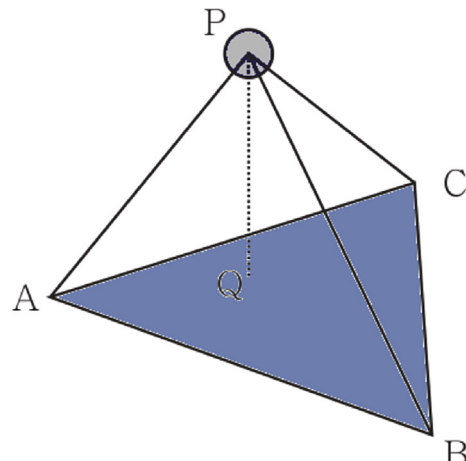


Fig. 12. Diagram of ship–ice contact search model.

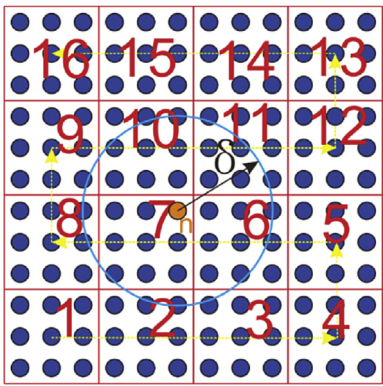


Fig. 13. Diagram of link-list search.

Table 1
Main parameters of a standard container ship.

Principal dimension	Full-scale ship	Model
Length between perpendiculars	230.0 m	4.3671 m
Breadth	32.2 m	0.6114 m
Designed draft	10.8 m	0.2051 m

To simplify the notation, we denote ξ as the relative position, which is

$$\xi = \mathbf{x}' - \mathbf{x}, \quad (2)$$

and their relative displacement is denoted by η ,

$$\eta = \mathbf{u}(\mathbf{x}', t) - \mathbf{u}(\mathbf{x}, t). \quad (3)$$

Here, the vector $\xi + \eta$ describes the relative position of the particles \mathbf{x}' and \mathbf{x} in the current configuration. Peridynamics is analogous to molecular dynamics, where the interaction between material points \mathbf{x}' and \mathbf{x} is called a bond, which one can view as a spring in the case of elastic interaction. The property of a bond that shows interaction over a finite distance is a fundamental difference between peridynamics theory and classical theory.

The horizon δ , a positive constant for a specific case, is an essential concept of peridynamics. The equation

$$|\xi| > \delta \Rightarrow \mathbf{f}(\eta, \xi) = 0, \quad (4)$$

shows that when the distance between material points \mathbf{x} and \mathbf{x}' is greater than δ , i.e., material point \mathbf{x}' is beyond the horizon of \mathbf{x} , the interaction linking \mathbf{x} and \mathbf{x}' vanishes. As shown in Fig. 1, H_x denotes the spherical neighborhood of \mathbf{x} with radius δ .

To simulate spontaneous fracture in a deformation body, bond failure is introduced in the material model presented above. It will be assumed for simplicity that the scalar bond force f depends only on the bond stretch, defined by

$$s = \frac{|\xi + \eta| - |\xi|}{|\xi|} = \frac{y - |\xi|}{|\xi|}. \quad (5)$$

Note that s is positive while the bond is in tension, and such a material is isotropic, since there is no dependence on the direction of ξ .

The simplest way to define failure into a constitutive model is by making bonds to fail as their deformation, i.e., stretching or compressing, is beyond a predetermined value. Once failure occurs, there will be no force in the bond, permanently. In other words, when a bond fails, it is dead forever, so the model is history-dependent. Considering the prototype micro-elastic brittle (PMB) material (Silling and Askari, 2005) the bond force can be defined by

$$f(y(t), \xi) = g(s(t, \xi))\mu(t, \xi), \quad (6)$$

where g is the linear scalar-valued function given by

$$g(s) = cs, \quad (7)$$

where c is a constant and μ is a history-dependent scalar-valued function that takes on values of either 1 or 0,

$$\mu(t, \xi) = \begin{cases} 1 & \text{if } s(t', \xi) < s_0 \\ 0 & \text{otherwise} \end{cases}, \quad (8)$$

where s_0 is the extreme stretch for a broken bond, whose value for the moment can be seen as a constant. One advantage of introducing failure at the bond level is that it leads to an unambiguous notion of local damage at a point, which is defined as

$$\varphi(\mathbf{x}, t) = 1 - \frac{\int_H \mu(\mathbf{x}, t, \xi) dV_\xi}{\int_H dV_\xi}. \quad (9)$$

3. Micro-parameters determined

The elasticity modulus, Poisson's ratio, viscosity factor, ultimate bending, and compression strength are crucial in numerical simulation to define the physical-mechanical properties. In peridynamics, these properties are defined by special micro-parameters such as bond constant and critical stretch. Model testing is an efficient approach to determine these parameters for the ice, where micro-parameters are adjusted to cater to the macro property of the specimens to achieve more accurate numerical models for subsequent research.

Two typical model tests, the uniaxial compression and three-point bending tests, which were conducted by Wang et al. (2014) and Ji et al. (2011) for Bohai Sea ice in winter, are simulated under the assumption that ice is an isotropic PMB material. As described in bond-based peridynamics, the relationship between strain and stress is defined by the bond constant, while the compression and bending strengths are reflected by the ultimate stretch of the bond.

The uniaxial compression model test is shown in Fig. 2, in which the size of specimen is $70 \times 70 \times 175$ mm and the load is performed by a plate-loading indenter aided by a hydro cylinder. Force is measured during the loading process, and the compression strength takes the value of the maximum stress when the fracture occurs.

$$\sigma_c = \frac{F_{\max}}{a^2} \quad (10)$$

The result of the simulation of the uniaxial compression test is shown in Fig. 3. The numerical model of the specimen is established by $14 \times 14 \times 35$ uniformly sized particles. The loading indenter is built up by three levels of particles moving at a constant velocity 0.02 m/s to model the compression effect. The summation of the bond forces that exert on the indenter model is outputted as the loading force, from which we can get the compression strength by eq. (10).

In the situation of compression, the failure mode of the bond is only in terms of compression failure, which is governed by the ultimate deformation in compression. Multi-groups of micro-parameters are attempted. The typical stress-strain curves from a model test and a simulation are plotted in Fig. 4.

A three-point bending model test is shown in Fig. 5, in which the size of the specimen is $75 \times 75 \times 700$ mm with a 5mm spacing between material points. In accordance with the mechanical characteristics of a simply supported beam, the loading force is denoted by P , which is determined by the maximum normal stress,

$$\sigma_f = \frac{3PL_0}{2bh^2}. \quad (11)$$

Fracture occurs when bending normal stress reaches a maximum

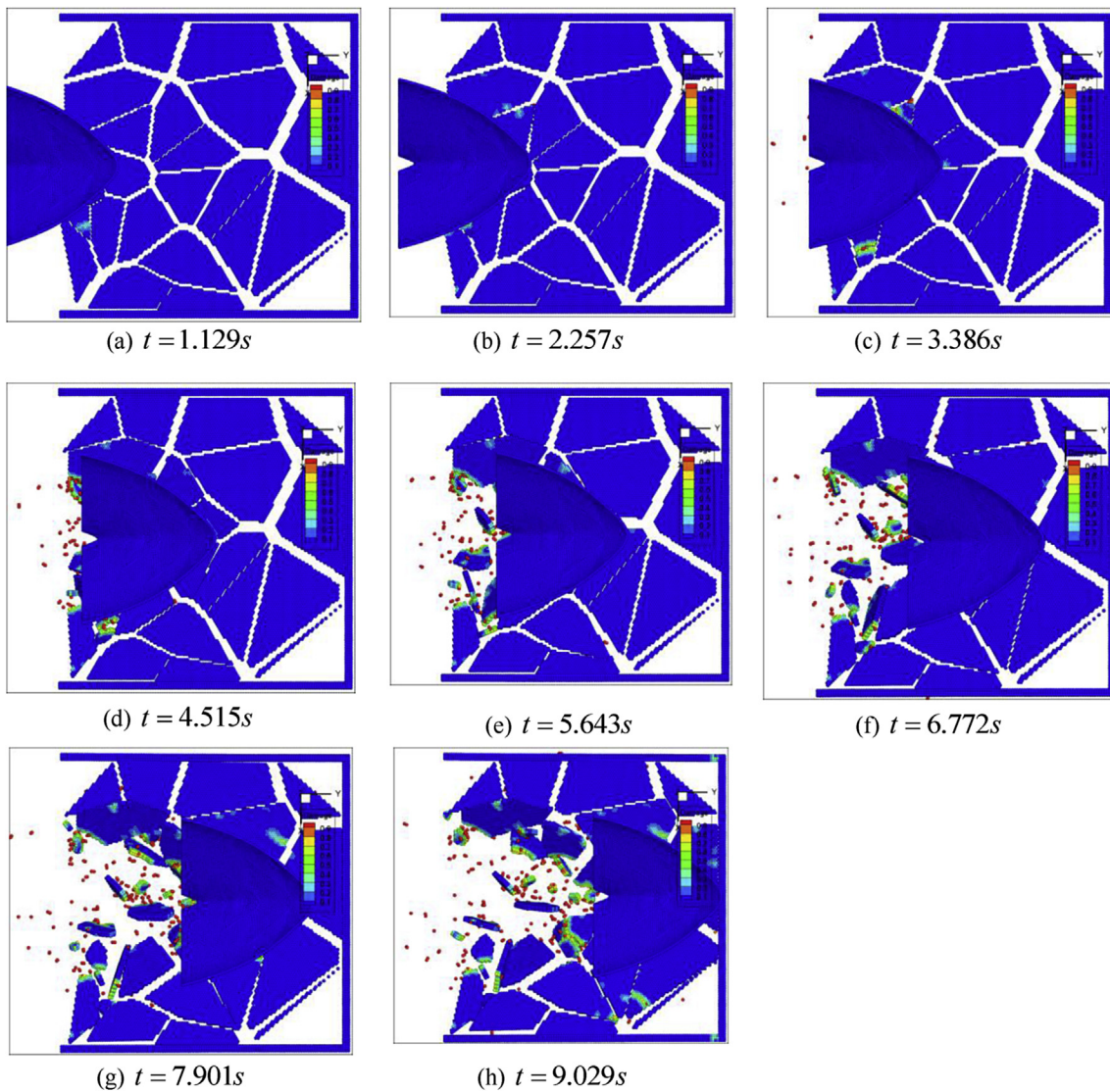


Fig. 14. Top view of broken ice navigation.

which is accepted as bending strength. Unlike compression, two kinds of bond deformations simultaneously exist in the three-point bending test. Considering that the bending strength and compression strength are unequal, another micro-parameter ultimate stretch in tension is introduced. The typical stress-time curves from a model test and numerical simulation are plotted in Figs. 6 and 7, respectively.

Fig. 6 shows the load-time plot for this simulation. It is observed that once the damage commences, the load carrying capacity of the beam drops very sharply to zero, indicating an elastic brittle damage type of response. Fig. 7 displays the spatial distribution of the damage variable over the beam with the loading indenter particles moving at a constant velocity 0.02 m/s. From the contour plot shown in this figure, it can be seen that damage initiation takes place in the tension zone at bottom also, simultaneously with development of compression damage at the top.

Ultimately, combining the results of the uniaxial compression and three-point bending tests, a sufficient numerical model of ice material is established, with two different ultimate stretches of bonds. The bond force as a function of bond deformation in the ice material model is shown in Fig. 8, with micro-parameters $E = 1.8 \text{ GPa}$, $S_{0c} = 0.003133$, and $S_{0b} = 0.000625$. These parameters are used in the subsequent study, and they imply that the compression strength and bending strength are 5.6 MPa and 1.125 MPa, respectively. We have now developed the constitutive relation we sought, and we will investigate it in a numerical

example. The possible range of parameters is collected and the characteristics which can be only described ice in Bohai sea at -9.1°C or ice in some other regions with similar mechanical properties.

To further validate the deformation response of the model mentioned above with FEM, uniaxial and cantilever beam tests subjected to a quasi-static tension loading of $F = 500 \text{ N}$ and $F = 5 \text{ N}$ are studied, respectively. The peridynamic discretization parameters are the same as before, except for the applied loading and time integration scheme with adaptive dynamic relaxation. The external applied loading is introduced in the form of a body force density in the boundary layer region. The results are plot in Figs. 9 and 10.

4. Preparation for ship-ice contact

4.1. Ice rubble model

Voronoi diagram classification is used for polygon segmentation, which is similar to the distribute the ice rubble in a channel. In a two-dimensional space, the Voronoi diagram is for a plane with n discrete points. The plane is divided into n zones, each consisting of a point, and the zone occupied by the points is a set of the closest points (Imelińska et al., 2000). It is defined as follows:

$$\forall p_i \in V, \quad V = |p_1, p_2, \dots, p_n|, \text{ we have}$$

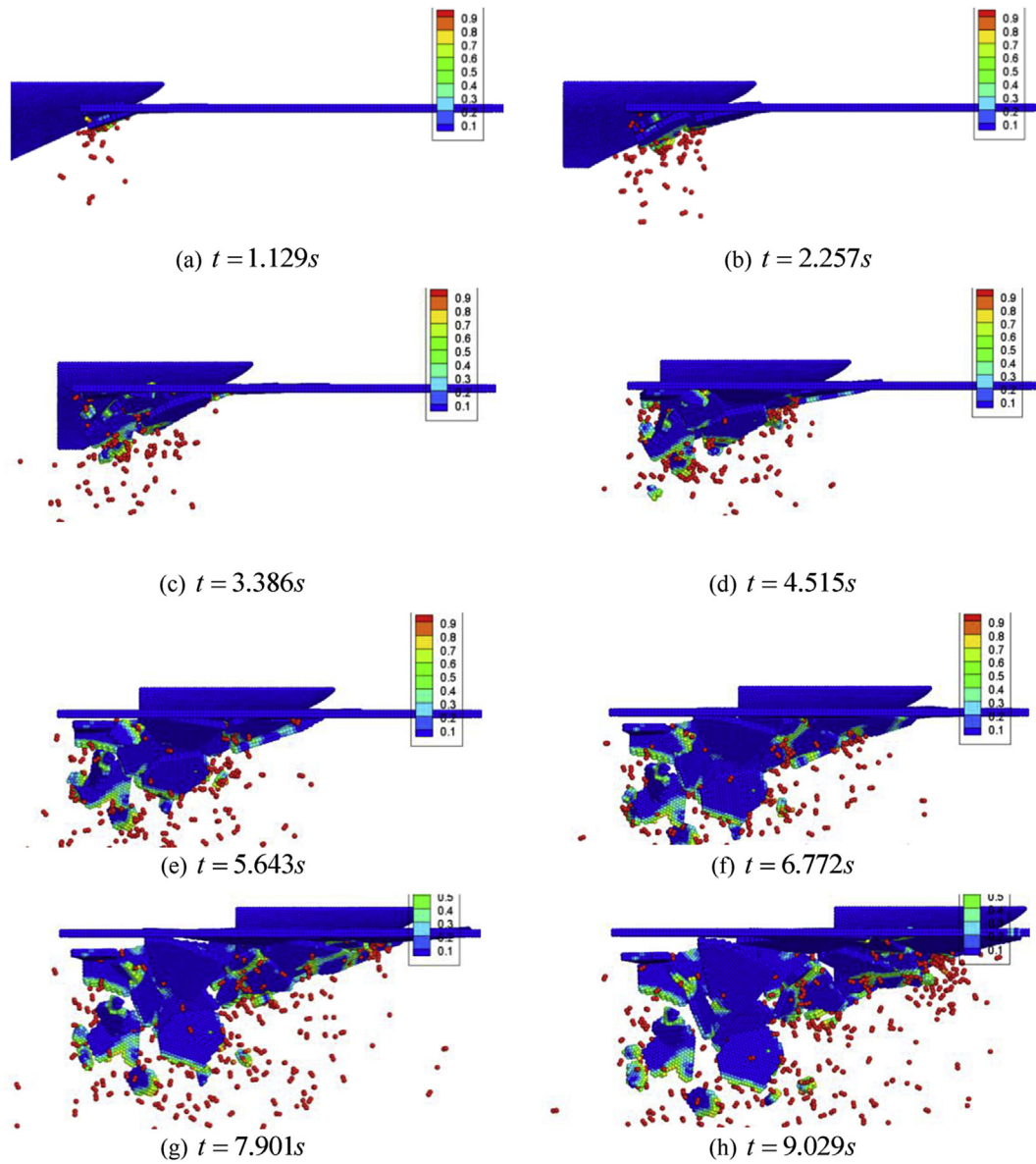


Fig. 15. Side view of broken ice navigation.

$$Vor(p_i) = \left\{ x \in R^2 \mid d(x, p_i) \leq d(x, p_j), \forall j \neq i, 1 \leq j \leq n \right\} \quad (12)$$

where $d(p, x) = \sqrt{(p_1 - x_1)^2 + (p_2 - x_2)^2}$ is the distance from point $p = (p_1, p_2)$ to point $x = (x_1, x_2)$.

Also, the Voronoi diagram for three dimensions is

$$Vor(p_i) = \left\{ x \in R^3 \mid d(x, p_i) \leq d(x, p_j), \forall j \neq i, 1 \leq j \leq n \right\} \quad (13)$$

The method is applied to scatter some random points to a given region. A convex polygon with the same edges as the number of the random points can also be generated according to the Voronoi diagram algorithm. The area of a given channel is known, and the distribution density and the average scale of ice rubble can be obtained from statistical data. Then the amount of ice rubble can be obtained and the number of random points which is the same as the quantity of ice rubble, and the polygon of ice rubble can be obtained using the Voronoi diagram algorithm. The corresponding ice-rubble model can then be obtained by filling each zone with the material points. Fig. 11 shows a model of a channel covered with ice rubble with concentration of 0.8. The average size of ice rubble is

$30 m^2$, with 51,200 material points, and the volume of each material point is $0.015625 m^2$. The different colors of the ice rubble represent the different material numbers produced by the Voronoi diagram algorithm.

4.2. The gravity and buoyancy of ice rubble

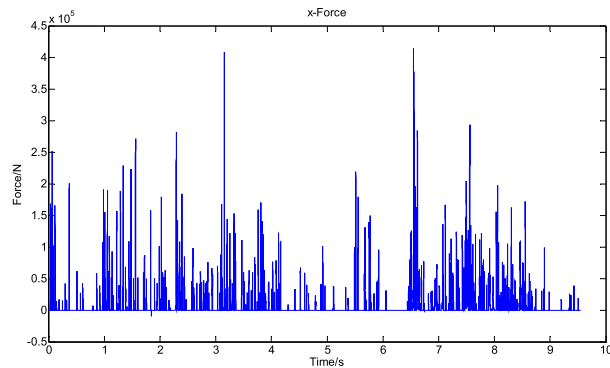
The gravity is balanced with the buoyancy of an ice block in calm water, and when a ship is considered, the ice block deviates from its equilibrium position, causing an imbalance of gravity and buoyancy and therefore having a further impact on the ice block movement. In this investigation, the buoyancy acting on ice block is approximately linearly affect the point's position. Consequently, the result Δf of gravitational force density g and volume force density B of a material point changes linearly with the change of the position.

If the material point is completely below the waterline, we have

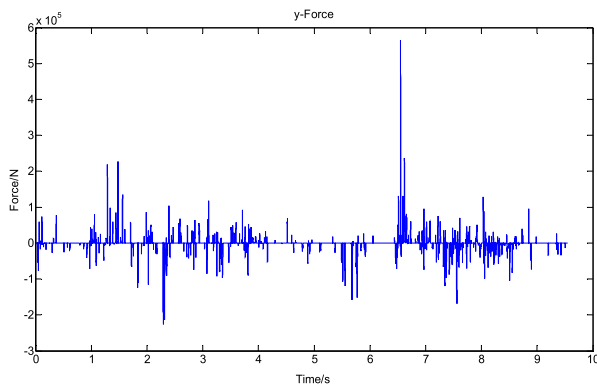
$$\Delta f = -g\rho_i + g\rho_w. \quad (14)$$

If the material point is completely above the waterline, we have

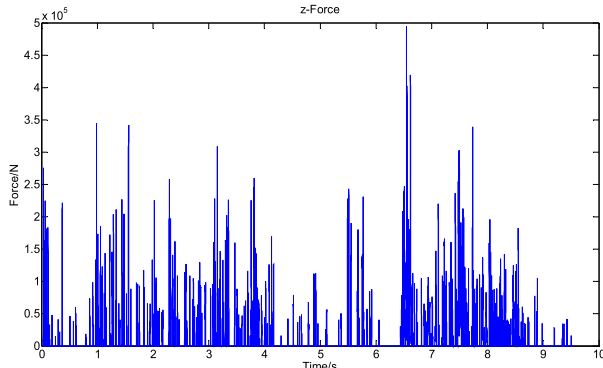
$$\Delta f = -g\rho_i. \quad (15)$$



(a) Historical force-time curve in x-axis



(b) Historical force-time curve in y-axis



(c) Historical force-time curve in z-axis

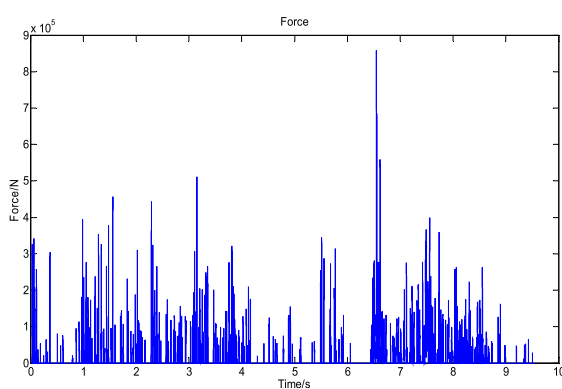


Fig. 16. Historical force-time curve for sailing in channel.

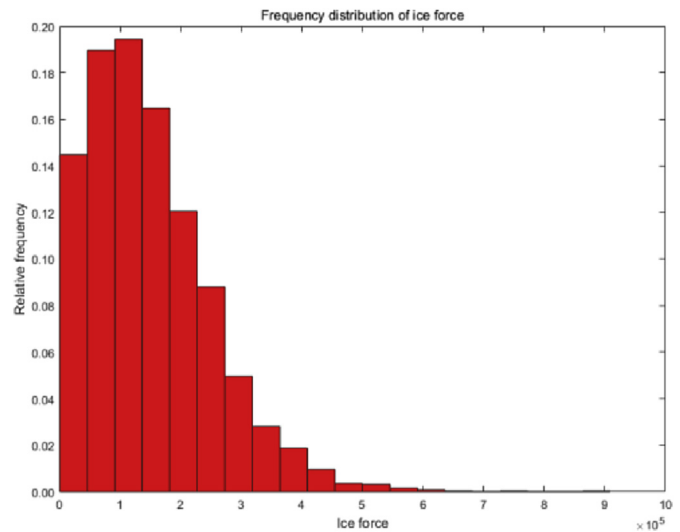


Fig. 17. Frequency map of ice force obtained by numerical simulation.

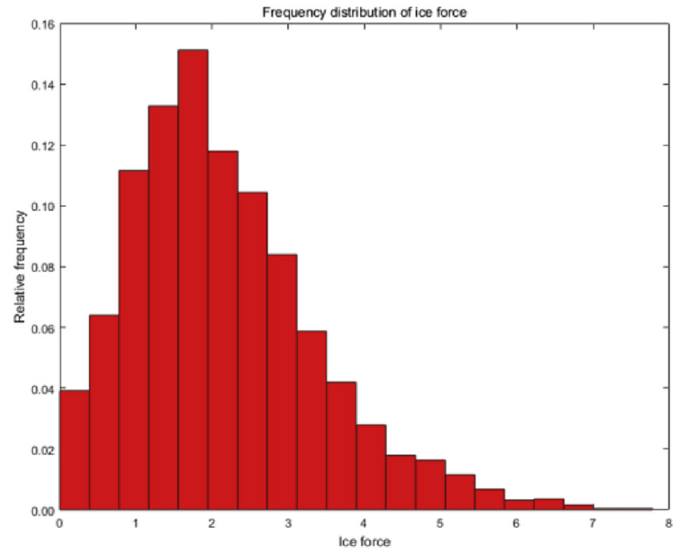


Fig. 18. Frequency map of ice force obtained by experiment.

For other circumstances, we have

$$\Delta f = -g\rho_i + g\rho_w l_w / \Delta, \quad (16)$$

where ρ_i is the density of ice, ρ_w is the density of water, l_w is the length of material point immersion water, and Δ is the scale of a material point.

4.3. Ship–ice contact model

A new material points contact algorithm improved from Di (2015), is introduced in peridynamics, using points contact triangle elements. A triangle element has three material points A, B and C as its vertices, as shown in Fig. 12.

The contact process is divided into two stages, called the first contact judgment and the second contact judgment.

The first judgment is to judge whether particle P and triangle ABC contact. When the distance between particle P and the plane of triangle ABC is less than the particle radius, whose value is equal to $dx/2$, contact occurs, assuming the particle is spherical. The distance of the particle P

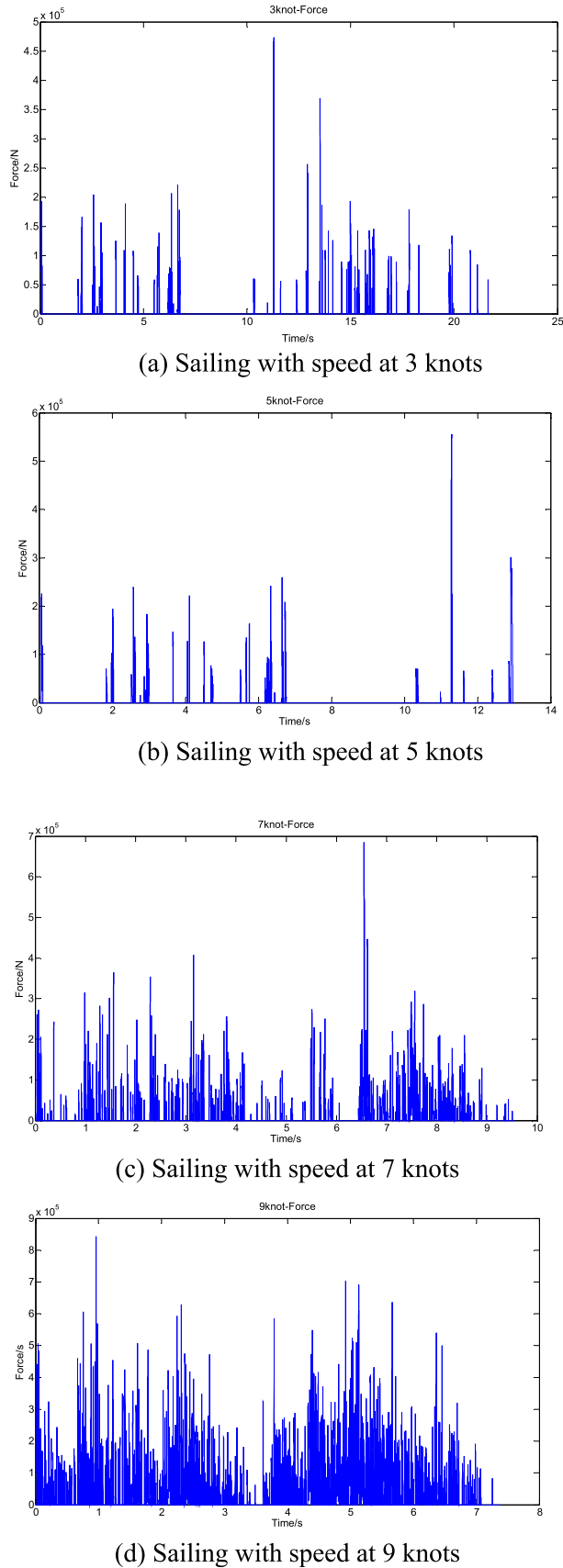


Fig. 19. Historical force-time curve for sailing with different speeds.

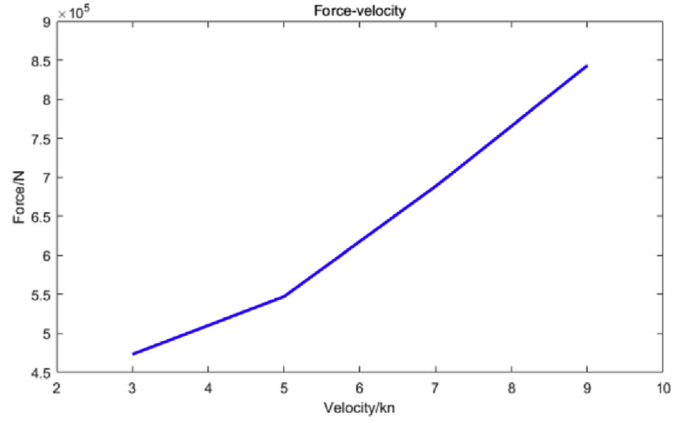


Fig. 20. Plot of maximum ice force against speeds.

and the plane ABC is defined in eq. (17) and the critical distance is defined in eq. (18):

$$|\mathbf{p}| = \mathbf{PA} \frac{\mathbf{BA} \times \mathbf{CB}}{|\mathbf{BA} \times \mathbf{CB}|} \quad (17)$$

$$|\mathbf{p}| < dx, \quad (18)$$

where dx is the radius of the material point, $\mathbf{p} = \mathbf{PQ}$.

If the first judgment cannot be satisfied, the particle has no chance to contact the plane in which the triangle unit is located, and the particle definitely does not contact the unit. When the first contact judgment is satisfied, it is necessary to further judge whether the particle has contact with the unit, which is the second contact judgment. This step is to determine whether the projection point Q of the particle P is inside triangle ABC; if point Q is inside triangular region ABC, the contact occurs, and otherwise it will not touch it. In this paper, the center-of-gravity method is used to determine whether the projection point Q is inside the triangular element. For any point in the plane, Q must have the following relations

$$\mathbf{d} = u\mathbf{a} + v\mathbf{b} \quad (19)$$

where $\mathbf{d} = \mathbf{AQ}$; $\mathbf{a} = \mathbf{AC}$; $\mathbf{b} = \mathbf{AB}$; and u and v are coefficients defined by eqs. (20) and (21), respectively:

$$u = \frac{(\mathbf{b} \cdot \mathbf{b})(\mathbf{p} \cdot \mathbf{a}) - (\mathbf{b} \cdot \mathbf{a})(\mathbf{p} \cdot \mathbf{b})}{(\mathbf{b} \cdot \mathbf{b})(\mathbf{a} \cdot \mathbf{a}) - (\mathbf{b} \cdot \mathbf{a})(\mathbf{a} \cdot \mathbf{b})} \quad (20)$$

$$v = \frac{(\mathbf{a} \cdot \mathbf{a})(\mathbf{p} \cdot \mathbf{b}) - (\mathbf{a} \cdot \mathbf{b})(\mathbf{p} \cdot \mathbf{a})}{(\mathbf{a} \cdot \mathbf{a})(\mathbf{b} \cdot \mathbf{b}) - (\mathbf{a} \cdot \mathbf{b})(\mathbf{b} \cdot \mathbf{a})}. \quad (21)$$

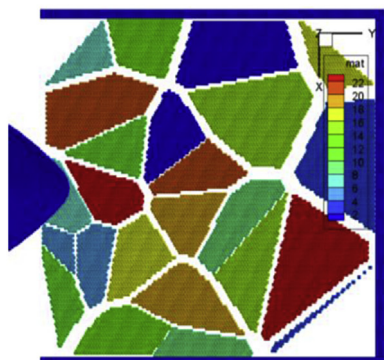
If projection point Q is in the interior of the triangle ABC, the two coefficients must satisfy the following conditions:

$$\begin{aligned} u &\geq 0 \\ v &\geq 0 \\ u + v &\leq 1 \end{aligned} \quad (22)$$

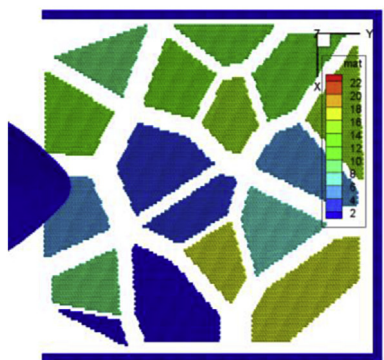
When contact occurs, the contact force is defined by the repelling short-range force (Silling, 2000). The force between two particles can be expressed as

$$\mathbf{f} = -\frac{\mathbf{p}}{|\mathbf{p}|} c_{sh} \left(\frac{|\mathbf{p}|}{r_{sh}} - 1 \right) \quad (23)$$

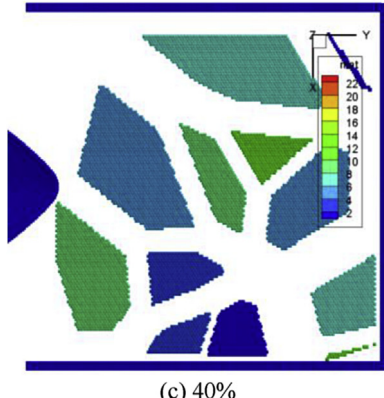
where c_{sh} is the short-range force constant and r_{sh} is the critical distance, beyond which the short-range force does not exist. The values of c_{sh} and



(a) 80%



(b) 60%



(c) 40%

Fig. 21. Diagrams of different concentrations of ice rubble.

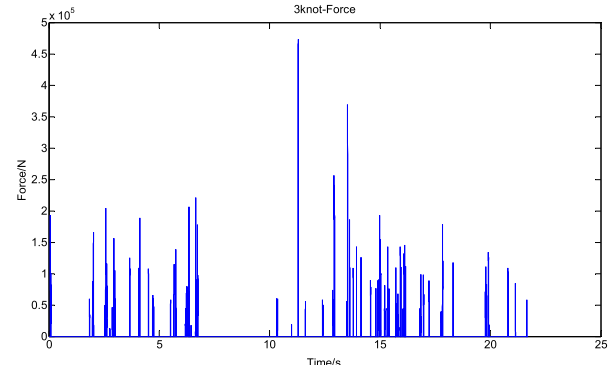
r_{sh} can be chosen as $c_{sh} = 5 \cdot c$ and $r_{sh} = \Delta/2$ (Madenci and Oterkus, 2014).

4.4. Family-member search with link list

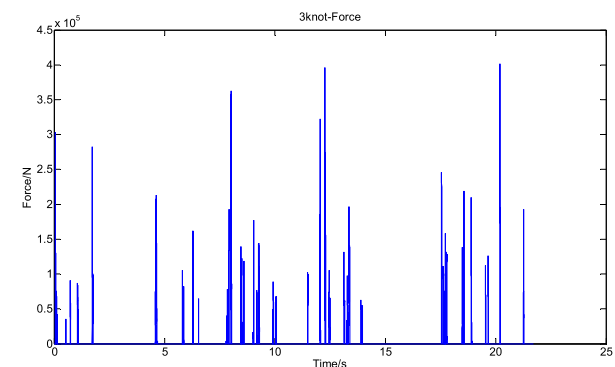
A family-member search for each main material point can be made very effectively while partitioning the body into many regions. Doing this can dramatically reduce the time spent in search of family members. Such a significant time reduction allows us to model very complex three-dimensional structures in peridynamics (Madenci and Oterkus, 2014).

Taking two-dimensions as an example, to achieving this time reduction, a body, which consists of many material points, should first be partitioned into many grids, with sides that are 3.0 times Δx , as shown in Fig. 13. Generally, the horizon value is set to $\delta = 3.015 \cdot \Delta x$, showing acceptable accuracy and efficiency (Silling and Askari, 2005).

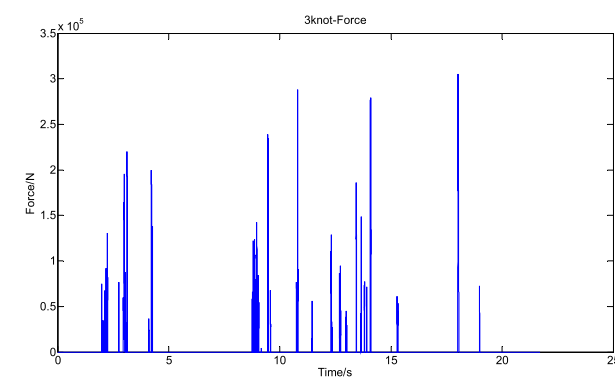
If material point n in grid 7 searches its family member points, the search process need only cover grid 7 and its neighboring grids, i.e. 1, 2,



(a) Sailing in channel with concentration of 80%



(b) Sailing in channel with concentration of 60%



(c) Sailing in channel with concentration of 40%

Fig. 22. Historical force–time curves with different concentrations of ice rubble.

3, 6, 7, 8, 9, 10 and 11, rather than searching all the material points that make up the body.

5. Validation of numerical cases

5.1. Simulation of ship navigation in ice rubble

The selected ship sailing in ice rubble with thickness of 0.5m, or navigating after an icebreaker sailing in level ice with thickness of 0.5m, is an ice-strengthened container ship. A resistance test using a model ship was carried out by Guo et al. (2016) in a towing tank. The main parameters of this standard container ship and the model are shown in Table 1.

The first case is for a channel covered with ice rubble with concentration of 0.8 and average size of $30 m^2$. The container ship has a speed of 7 knots. The result and the historical force–time curve are shown in

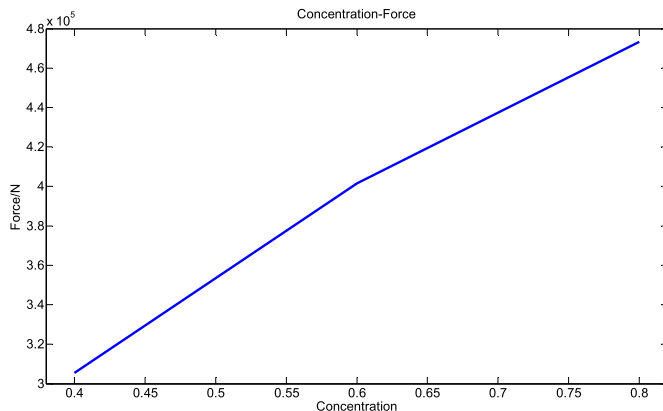


Fig. 23. Plot of maximum ice force against concentration.

Figs. 14–16, respectively.

To simplify the calculations, the bow model is set up only for the section of the ship–ice contact zone by continuously arranged particles. The interaction is formulated by means of the bow model moving at a uniform velocity, then the ice load $F(t)$ is the summation of the short-range forces exerted on bow material points. A historical force–time curve can be achieved by outputting the summation,

$$F(t) = \sum_1^{ns} \sum_1^{ni(t)} f_{sh} \cdot V, \quad (24)$$

where $F(t)$ is the ice load in t^{th} time step, ns is the number of ship material points, $ni(t)$ is the number of ice material points that interact with the ship in the t^{th} time step, f_{sh} is the contact force density obtained by eq. (23), and V is the volume of the ice material point.

Figs. 14 and 15 show that this method successfully simulated the container ship sailing in the ice rubble. At the beginning, the ice rubble moved forward in the horizontal direction owing to contact with the ship. It is apparent that some ice rubble has accumulated in the bow of the ship as the long-term effect of the ship–ice contact process. Accompanied by this process, broken ice has overturned due to the vertical force, these pack ice fully in contact with the bow surface, and broken ice blocks slip from the bow to the outside, where they can move freely, such as the bottom and sides far from the hull, resulting from the relative motion between the ice and the hull's surface. It is worth noting that in the process of ice contacts with the hull, because the speed is high enough and the size of some ice rubble is large, the rotation of ice rubble is insufficient to offset the overturning response of ship–ice contact, so some large ice blocks will be broken further. However, the amplitude of breaking ice blocks movement is larger than practice observed in ice tank, this is partly because the effect of water is not considered enough. Compared with the continuously breaking ice in level ice, although there is ice broken in both patterns, sailing in a channel covered with ice rubble shows more continuous and stochastic characteristics. Additionally, the red particles in the above pictures are a non-physical phenomenon in peridynamic numerical simulation, which has not yet been solved with a reasonable approach. The authors hold believe these red particles are natural phenomena, because many segments are tiny or invisible to the naked eye when an ice block is broken.

The historical force–time curve for continuous breaking mode is shown in Fig. 16.

The result plotted in Fig. 16 shows that the ice force during the process of ice breaking in ice rubble is distinct from the ice force in the process of continuous ice breaking in level ice. It has an obvious periodic characteristic, but it shows more randomness and relative continuity. At a concentration of 80%, the average size of the crushed ice is 30 m^2 , the ice thickness is 0.5 m , and the ship is sailing at 7 knots. The maximum ice

force reaches 0.85813 MN , and the peak value of the ice–force interval appears in pulse form. The peak value shows random characteristics with the randomness of ice rubble. The ice force in the x-axis and z-axis shown in Fig. 16(a) and (c) show a similar trend with the total ice force in Fig. 16(d), while the horizontal ice force in the y–axis shown in Fig. 16(b) shows asymmetry on both sides, which is a result of the random arrangement of ice rubble.

The frequency maps of ice force obtained by numerical simulation and experiment are shown in Figs. 17 and 18, respectively. The overall trends of frequency in Figs. 17 and 18 are consistent, but the frequency peak is offset. We believe a reason for that lies in the difference resulting from the real ice and synthetic ice. The magnitude of the horizontal ice force reaches the order of 10^5 N , which shows a good agreement with the full-scale result predicted result by Guo et al. (2016).

5.2. Influence of speed on ice load of ice breaking

We examined the case of a channel covered with ice rubble with a concentration of 60%, ice thickness of 0.5 m , and an average size of ice rubble of 10 m^2 . Four computational conditions were established, with speeds of 3, 5, 7, and 9 knots. The resulting historical force–time curve is shown in Fig. 19.

Fig. 19 shows that as the speed increases, so does the frequency of ice load. The ice force at a speed of 9 knots is almost continuously in contact with the hull. In addition, when the speed increases, the maximum ice load is increases. Fig. 20 shows that the trend of maximum ice force of these four groups varies with the speed. As the speed increases, the time of interaction between the hull and the ice rubble is less, and the kinetic energy of ice rubble is greater, which is why the ice force increases with the speed. The maximum ice force at 9 knots is 1.8 times that at a speed of 3 knots, which differs from the result predicted by Guo et al. (2016) which was about 3.6, but showing good agreement with the work done by Kim et al. (2009). Further increasing the speed will increase the ice force to a dangerous level, so a reasonable speed should be guaranteed during ice-breaking.

5.3. Influence of concentration on ice load of ice breaking

In this case, the container ship sails at a speed of 3 knots, the channel is covered with ice rubble of average size 30 m^2 , and the thickness of the ice is 0.5 m . A comparative analysis was performed of the effect of different concentrations of ice rubble on ice load in a channel with concentration of 40%, 60%, and 80%. Channels covered with different concentrations are shown in Fig. 21. The historical fore–time curves are shown in Fig. 22.

The concentration of ice rubble has a significant effect on the frequency of ice force and the maximum ice load. The frequency of ice load shows an increase as the concentration of ice rubble rises. The amplitude of ice force greater than 10^5 N with concentration of 80%, 60%, and 40%, is 31, 22, and 13 times, respectively. This phenomenon occurs because the probability of collision between ship and ice decreases as the concentration decreases. In these three cases, the maximum ice forces are 473280, 401510, and 305400 N, respectively. Fig. 23 shows that the tendency of the maximum ice force varies according to concentration, and the maximum ice force sailing in a concentration of 80% is 1.55 times that in a concentration of 60%, which agrees with the result of Guo et al. (2016) in a certain range.

5.4. Influence of average size of ice rubble on ice load of ice-breaking

In this case, the container ship sails with a speed of 7 knots in a channel covered with ice rubble with a concentration of 80%, and the thickness of the ice is 0.5 m . We comparatively analyze the effect of average size of ice rubble on the ice load, with values of 10, 15, 20, 25, 30, 35, and 40 m^2 , respectively. The diagrams of different average sizes of

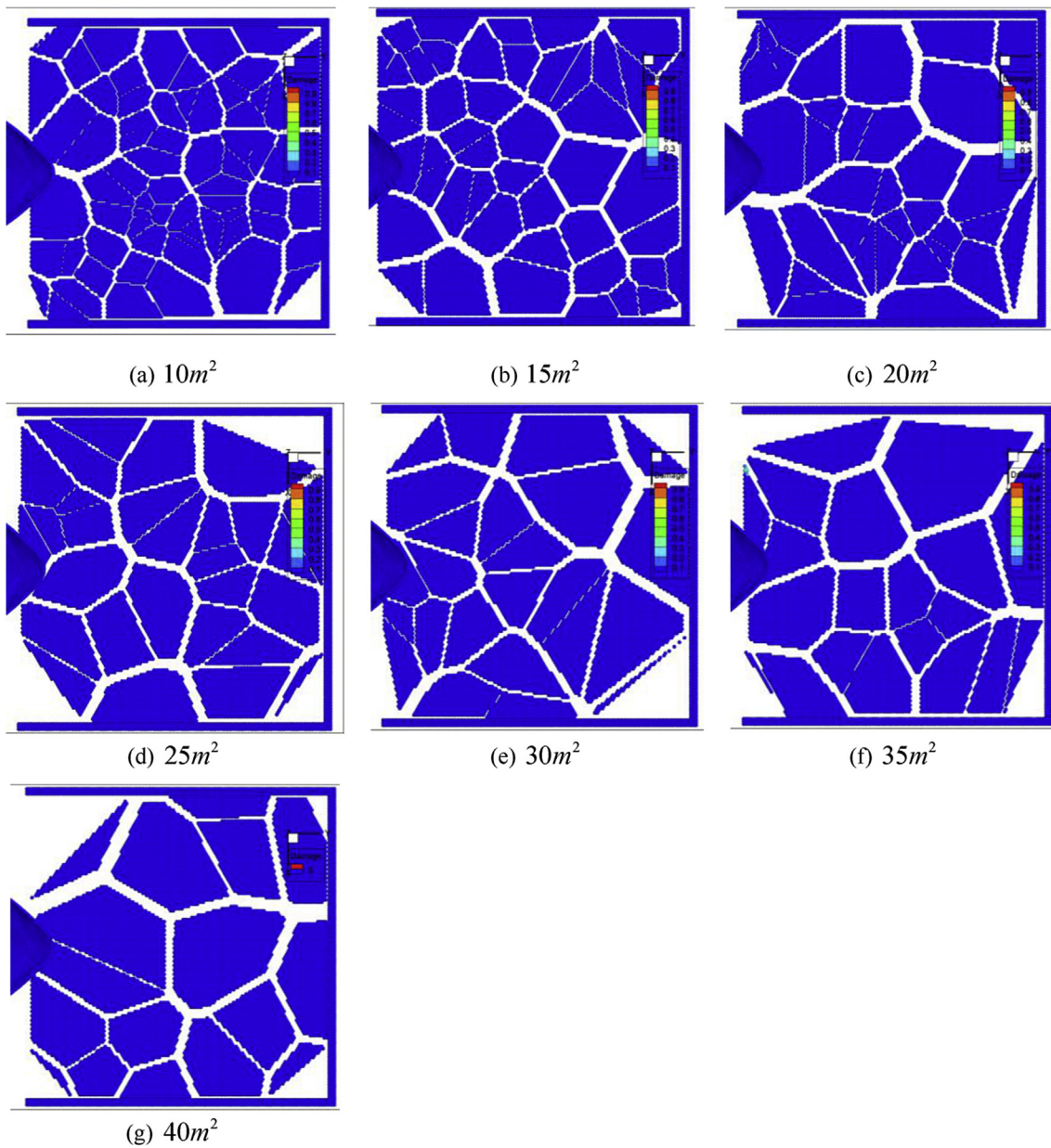


Fig. 24. Diagrams of different average sizes of ice rubble.

ice rubble are shown in Fig. 24. The historical force–time curves of sailing in different average sizes of ice rubble are shown in Fig. 25. The maximum ice force of sailing in different average sizes is shown in Fig. 26.

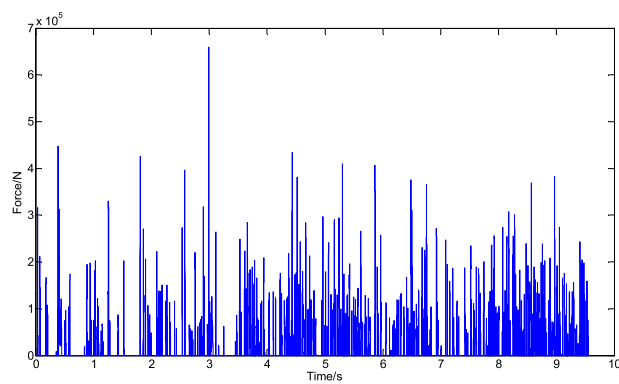
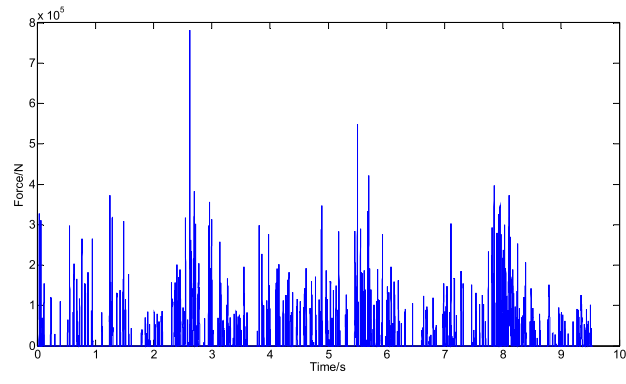
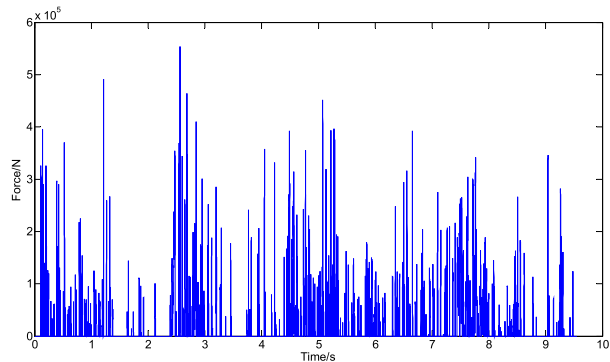
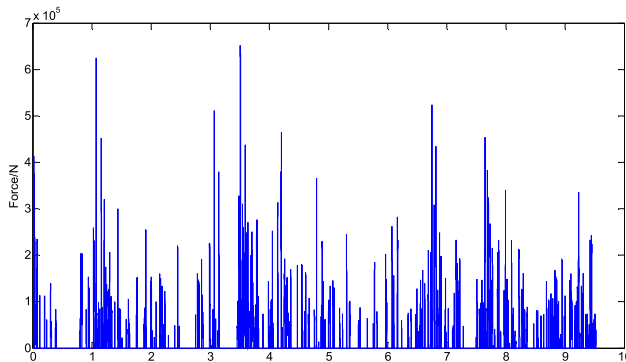
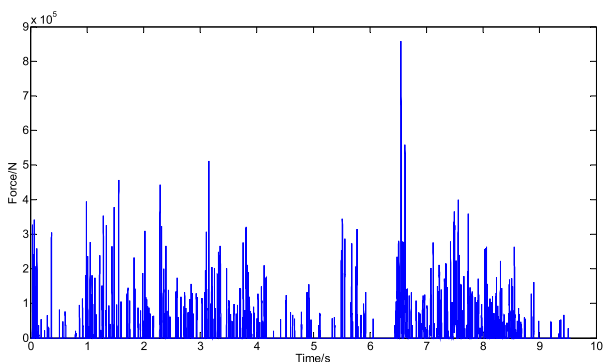
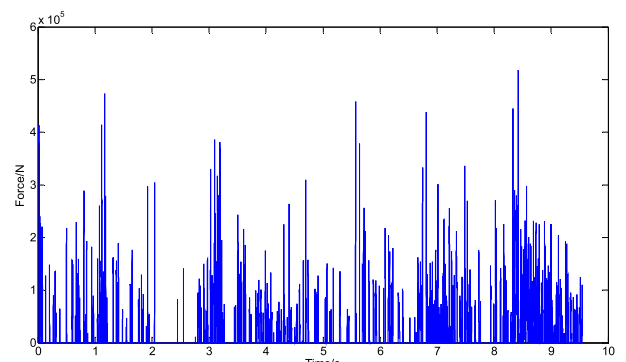
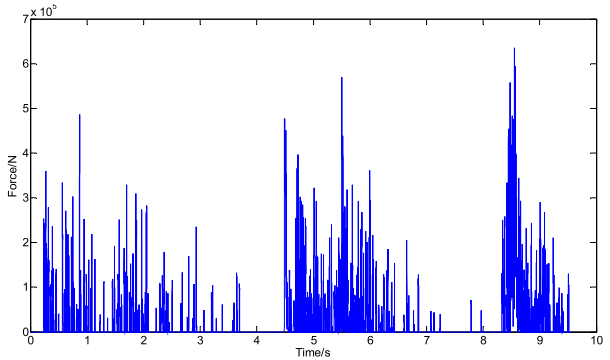
Fig. 25 shows that as the average size of ice rubble rises, the frequency of ice force decreases, which can be interpreted as the amount of ice rubble growing as its average size drops. Fig. 26 shows that with the concentration of ice rubble fixed, the maximum ice force fluctuates in a certain range with different average sizes of ice rubble. For example, with a concentration of 80%, the maximum ice force of different average sizes of ice rubble on the ship is between 51829 N and 85813 N, with a mean value of 665740 N, which shows good agreement with the result by Guo et al. (2016).

6. Conclusions

Peridynamics is first introduced to model ship–ice contact, and the ice rubble is modeled using a Voronoi diagram algorithm. Ice load and the characteristics of the ice-breaking process are successfully captured

while sailing in a channel with different concentrations and average sizes of ice rubble, although the gravity and buoyancy of ice are not given enough consideration. From simulation results, the following conclusions can be drawn.

- (1) The critical bond length, $s_{0c} = 0.003133$ and $s_{0b} = 0.000625$ obtained by choosing as an empirical value, which is modified along with a set of parameters to calibrate the experiment results of compression and bending, respectively, can describe the mechanical characteristics of ice.
- (2) Velocity shows a significant influence on the ice load. With increases in speed, the frequency of the ice load rose significantly, and the maximum ice force at a speed of 9 knots was 1.8 times that with a speed of 3 knots for an ice thickness of 0.5 m.
- (3) Concentration shows considerable influence on the frequency and magnitude of the ice force. The frequency of ice load shows an upward trend as the concentration of ice rubble rises, so does the magnitude of ice load. The maximum ice force sailing in

(a) Sailing in channel with average size of $10m^2$ (b) Sailing in channel with average size of $15m^2$ (c) Sailing in channel with average size of $20m^2$ (d) Sailing in channel with average size of $25m^2$ (e) Sailing in channel with average size of $30m^2$ (f) Sailing in channel with average size of $35m^2$ (g) Sailing in channel with average size of $40m^2$ **Fig. 25.** Historical force-time curves with different sizes of ice rubble.

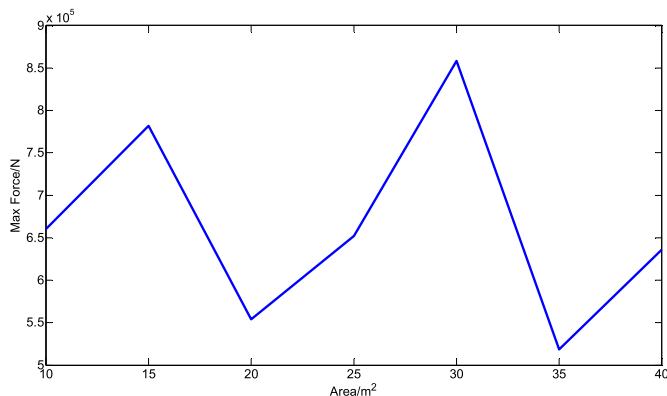


Fig. 26. Plot of maximum ice force against average size.

concentration of 80% is 1.55 times that in a concentration of 60% for ice thickness of 0.5 m.

- (4) The average size of ice rubble has a noticeable influence on the frequency of the ice load. As the average size of ice rubble rises, the frequency of the ice force becomes lower. However, with a fixed concentration of ice rubble, the maximum ice force fluctuates in a certain range with different average sizes of ice rubble.

Acknowledgements

This work is supported by the National Natural Science Foundation of China (Nos. 51579054 and 51639004).

Appendix A. Supplementary data

Supplementary data related to this article can be found at <https://doi.org/10.1016/j.oceaneng.2017.11.034>.

References

- Aksnes, V., 2010. A simplified interaction model for moored ships in level ice. *Cold Regions Sci. Technol.* 63 (1), 29–39.
- Daley, C., Tuhkuri, J., Riska, K., 1998. The role of discrete failures in local ice loads. *Cold Regions Sci. Technol.* 27, 197–211.
- Das, J., PolićD, Ehlers S., et al., 2014. Numerical simulation of an ice beam in four-point bending using SPH[C]. In: ASME 2014 33rd International Conference on Ocean, Offshore and Arctic Engineering. American Society of Mechanical Engineers. V010T07A013.
- Derradji-Aouat, A., Wang, J., 2010. Ship Performance in Broken Ice Floes - Preliminary Numerical Simulations, Institute for Ocean Technology. Report No. TR-2010-24. National Research Council, St. John's, NL, Canada.
- Di, S.C., 2015. Discrete Element Simulation of Ice Load on Offshore Platform and Ship Hull Based on GPU Parallel Algorithm. Dalian University of Technology.
- Eranti, E., 1991. General theory of dynamic ice structure interaction with applications. *Proc. First Int. Offshore Polar Eng. Conf.* 489–498.
- Eranti, E., 1992. Dynamic Ice Structure Interaction. Helsinki University of Technology, Espoo, Finland.
- Guo, C.X., Xie, C., Wang, S., et al., 2016. Resistance of Ships in Pack Ice Conditions. *J. Harbin Eng. Univ.* 37 (4), 481–486.
- Imelińska, C., Downes, M.S., Yuan, W., 2000. Semi-automated color segmentation of anatomical tissue. *Comput. Med. Imaging Graph. Off. J. Comput. Med. Imaging Soc.* 24 (3), 173.
- Ji, S.Y., Wang, A.L., Su, J., et al., 2011. Experimental test and characteristic analysis of sea ice bending strength around Bohai sea. *Prog. Water Sci.* 22 (2), 266–277.
- Jia, Z., Ulfvarson, A., Ringsberg, J.W., et al., 2009. A return period based plastic design approach for ice loaded side-shell/bow structures. *Mar. Struct.* 22 (3), 438–456.
- Kim, M.C., Lim, T.W., Jo, J.C., et al., 2009. Comparison study on the propulsion performance for icebreaker with synthetic ice and refrigerated ice. *한국해양공학회지 제23권 제1호* 23 (1), 129–134.
- Kim, M.C., Lee, S.K., Lee, W.J., et al., 2013. Numerical and experimental investigation of the resistance performance of an icebreaking cargo vessel in pack ice conditions. *Int. J. Nav. Archit. Ocean Eng.* 5 (1), 116–131.
- Kujala, P., 1991. Damage Statistics of Ice-strengthened Ships in the Baltic Sea 1984–1987. Winter Navigation Research Board:Finnish Board of Navigation & Swedish Administration of Shipping and Navigation. Technical Report No 50. Espoo, Finland.
- Kwok, R., Cunningham, G.F., 2012. Deformation of the Arctic Ocean ice cover after the 2007 record minimum in summer ice extent. *Cold Regions Sci. Technol.* 69 (1), 17–23.
- Lubbad, R., Løset, S., 2011. A numerical model for real-time simulation of ship-ice interaction. *Cold Regions Sci. Technol.* 65 (2), 111–127.
- Madenci, E., Oterkus, E., 2014. Peridynamics Theory and its Applications. Springer New York.
- Matlock, H., Dawkins, W.P., Panak, J.J., 1969. A Model for the Prediction of Ice-structure Interaction. Annual Offshore Technology Conference, Dallas, USA, pp. 687–694.
- Silling, S.A., 1998. Reformulation of Elasticity Theory for Discontinuous and Long-range Forces., SAND98-2176. Sandia National Laboratories, Albuquerque, NM.
- Silling, S.A., 2000. Reformulation of elasticity theory for discontinuities and long-range forces. *J. Mech. Phys. Solids* 48 (1), 175–209.
- Silling, S.A., Askari, E., 2005. A meshfree method based on the peridynamic model of solid mechanics. *Comput. Struct.* 83 (s17–18), 1526–1535.
- Song, Y.Y., Kim, M.C., Chun, H.H., 2007. A study on resistance test of icebreaker with synthetic ice. *J. Soc. Nav. Archit. Korea* 44 (4), 389–397.
- Wang, A.L., Xu, N., Ji, S.Y., 2014. Characteristics of sea ice uniaxial compressive strength around the coast of Bohai Sea. *Ocean Eng.* 32 (4), 82–88.